Applied Physics Letters

RESEARCH ARTICLE | NOVEMBER 21 2025

Magnetically enhanced quasi-zero-stiffness galloping harvester for efficient wind energy harvesting and autonomous sensing

Ye Zhang; Yawei Wang ; Yaozi Zheng; Chunbo Lan ; Guobiao Hu

Check for updates

Appl. Phys. Lett. 127, 203904 (2025)
https://doi.org/10.1063/5.0308844

View Online
Export Citation

Articles You May Be Interested In

Investigating the effect of surface protrusions on galloping energy harvesting

Appl. Phys. Lett. (April 2023)

Piezoelectric wind velocity sensor based on the variation of galloping frequency with drag force

Appl. Phys. Lett. (June 2020)

A novel energy harvester based on dual vibrating mechanisms with self-actuation

Rev. Sci. Instrum. (May 2023)

08 January 2026 14:58:50

AIP Publishing

AIP Publishing
Applied Physics Letters
Special Topics Open for Submissions
Learn More

Applied Physics Letters ARTICLE pubs.aip.org/aip/apl

Magnetically enhanced quasi-zero-stiffness galloping harvester for efficient wind energy harvesting and autonomous sensing

Cite as: Appl. Phys. Lett. **127**, 203904 (2025); doi: 10.1063/5.0308844
Submitted: 24 October 2025 · Accepted: 2 November 2025 ·
Published Online: 21 November 2025

View Online Export Citation CrossMark

Ye Zhang,[1] Yawei Wang,[1] Yaozi Zheng,[1] Chunbo Lan,[2] and Guobiao Hu[1,a)]

AFFILIATIONS

[1]Internet of Things Thrust, The Hong Kong University of Science and Technology (Guangzhou), Guangzhou, Guangdong 511400, People's Republic of China
[2]National Key Laboratory of Helicopter Aeromechanics, Nanjing University of Aeronautics and Astronautics, Nanjing, Jiangsu 210016, People's Republic of China

[a)]**Author to whom correspondence should be addressed:** guobiaohu@hkust-gz.edu.cn

ABSTRACT

This study presents an enhanced quasi-zero-stiffness galloping-based piezoelectric energy harvester (EQZS-GPEH) for efficient wind energy harvesting and self-powered wind speed sensing. It employs a five-magnet configuration to expand the QZS region, thus effectively reducing the cantilever beam stiffness, lowering the onset wind speed, and amplifying the dynamic response. The experimental results demonstrate that the EQZS-GPEH delivers a maximum power output of 1.55 mW at a wind speed of $U = 4.834$ m/s and a load resistance of $R_L = 0.7$ MΩ, representing a 294% improvement over the traditional galloping-based piezoelectric energy harvester (T-GPEH) and a 142% improvement over the conventional QZS galloping-based piezoelectric energy harvester (CQZS-GPEH). Beyond enhanced performance, the EQZS-GPEH also exhibits a highly linear relationship between vibration frequency and wind speed ($R^2 > 0.99$), enabling accurate wind speed estimation. Leveraging this characteristic, an analog-to-digital converter circuit was developed to process harvester output and estimate wind speed, achieving a relative error of <5% compared to reference instrumentation. Integrated with the EQZS-GPEH, this forms a fully self-powered wind speed sensing system. These results demonstrate the EQZS-GPEH as a high-performance self-sustaining solution for distributed energy harvesting and sensing, making it highly promising for future IoT applications.

Published under an exclusive license by AIP Publishing. https://doi.org/10.1063/5.0308844

08 January 2026 14:58:50

The Internet of Things (IoT), a key technology of the future, is reshaping industry and daily life through closed-loop systems that integrate sensing, communication, and edge computing, driving advances in areas such as intelligent manufacturing,[1] smart cities,[2] and healthcare.[3] However, reliance on chemical batteries for distributed devices poses environmental risks and high follow-up maintenance costs, making ambient energy harvesting an attractive and sustainable alternative.[4–7]

Wind, as a ubiquitous natural resource, can excite structural vibrations through flow-induced phenomena such as vortex-induced vibration (VIV),[8] galloping,[9] and flutter.[10] These vibrations can then be converted into electricity through piezoelectric, electromagnetic, or triboelectric transduction. Galloping is a self-excited aeroelastic instability whose amplitude increases with wind speed, making it highly suitable for broadband wind energy harvesting.[11,12] Piezoelectric transducers are widely adopted in such galloping energy harvesting systems because of their high power density, simple structure, and ease of integration.

Various strategies have been proposed to enhance the performance of galloping-based piezoelectric energy harvesters (GPEHs), such as adding small attachments,[13] designing multi-degree-of-freedom structures,[14] and introducing nonlinear magnetic forces.[15–18] In particular, magnetic coupling has been widely explored for developing high-performance energy harvesters due to its potential advantages in enhancing output power[19,20] and tuning structural dynamic characteristics.[21,22] Among various magnetic coupling configurations, certain designs enable the formation of quasi-zero-stiffness (QZS) regions,[23,24] which can result in favorable nonlinear dynamics for broadband and ultra-low frequency energy harvesting.[25,26] By appropriately introducing a QZS region, the GPEH can operate efficiently not only at low-wind speeds but also over an expanded operational bandwidth.[27,28] Moreover, GPEHs hold strong potential for environmental sensing,

Published under an exclusive license by AIP Publishing

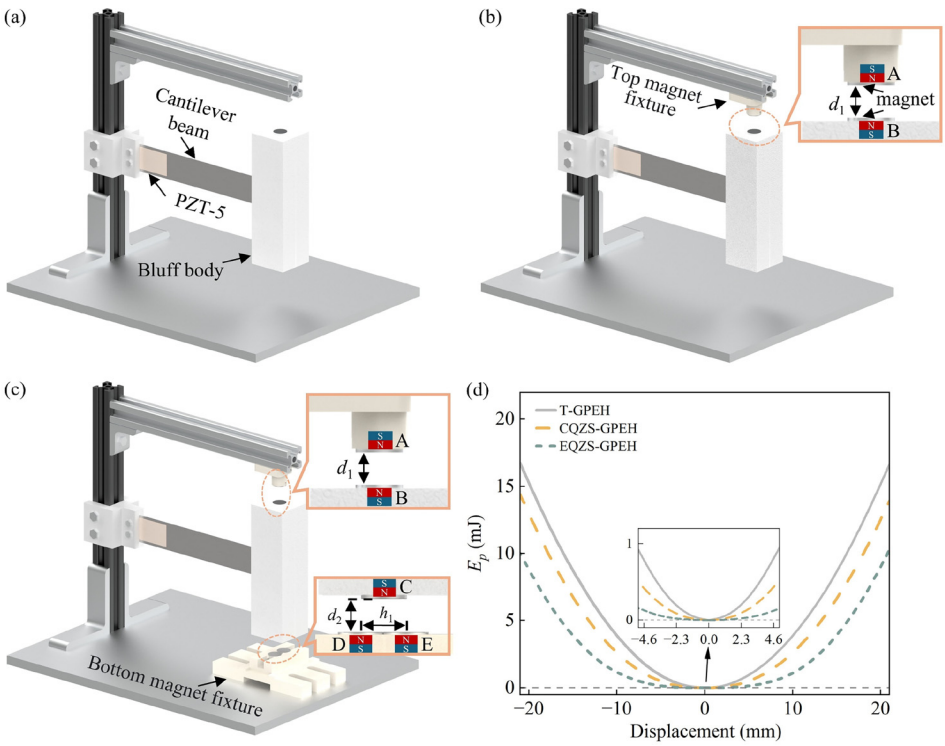

FIG. 1. (a) Traditional galloping-based piezoelectric energy harvester (T-GPEH); (b) conventional quasi-zero-stiffness GPEH (CQZS-GPEH); (c) enhanced quasi-zero-stiffness GPEH (EQZS-GPEH); and (d) potential energy (E_p) profiles of the three GPEH configurations.

as demonstrated by studies in which they powered temperature and humidity sensors, validating their great promise for self-powered sensing applications.[29–32]

Research on self-powered wind speed sensing using GPEHs remains limited, primarily due to the combined limitations of low energy output, high signal-processing power requirements, and ineffective energy management for practical applications. In this work, we present an enhanced quasi-zero-stiffness galloping-based piezoelectric energy harvester (EQZS-GPEH) integrated with an ultra-low-power analog-to-digital converter (ADC) to achieve a fully self-powered wind speed sensing system.

The proposed EQZS-GPEH [Fig. 1(c)] comprises a cantilever beam with a PZT-5 sheet bonded near its fixed end and a cuboid bluff body carrying magnets on its top and bottom surfaces. Removing the bottom magnets yields a conventional QZS galloping-based piezoelectric energy harvester [CQZS-GPEH, Fig. 1(b)], while further removing the top magnet reduces it to a traditional GPEH [T-GPEH, Fig. 1(a)].

By tuning the distance d_1 between magnet A and magnet B, the repulsive force can counteract the restoring force of the cantilever beam, thereby achieving a QZS region. Unlike the top magnet arrangement, magnets D and E are positioned beneath magnet C. This configuration of magnets further offsets the restoring force of the cantilever beam, enabling the QZS region to extend over a wider displacement range.

A monostable design is adopted for all three GPEHs to avoid multi-stable potential barriers and enhance energy harvesting efficiency. The distance between magnet A and magnet B (d_1) was set to 16 mm to ensure that the magnetic repulsive force provides sufficient stiffness softening without inducing an undesired deviation of the static equilibrium position. Based on a similar balance of stiffness modulation and stability considerations, the distance between magnet C and magnet D (d_2) was set to the same value. To make sure that the bluff body can overcome the repulsive force of the bottom magnets and achieve large vibration amplitudes, the distance between magnet D and magnet E (h_1) was set to 12 mm. This value corresponds to the minimum safe spacing relative to the magnet's radius, ensuring strong nonlinear interaction while avoiding excessive repulsive force. This value corresponds to the minimum safe spacing relative to the 6 mm magnet radius, ensuring strong nonlinear interaction while avoiding premature saturation of the repulsive force. Table I lists the shared physical parameters used in all three GPEH configurations.

The potential energy E_p can be generally obtained by integrating the restoring force $F_r(y)$ of the cantilever beam over the displacement range: $E_p = \int_{-y_0}^{y_0} F_r(y)dy$. As shown in Fig. 1(d), the potential energy of the EQZS-GPEH is markedly reduced by the five-magnet configuration, resulting in a distinct flat region where E_p approaches zero. For the CQZS-GPEH, a smaller zero-E_p region is observed near $y = 0$ due

TABLE I. The common physical parameters of three GPEHs.

Components	Dimensions
Cubic bluff body	$35 \times 35 \times 120\,\text{mm}^3$
Cantilever beam	$200 \times 25 \times 0.7\,\text{mm}^3$
PZT-5 sheet	$30 \times 20 \times 0.4\,\text{mm}^3$
Circular magnets	$6^2\pi \times 3\,\text{mm}^3$

08 January 2026 14:58:50

Published under an exclusive license by AIP Publishing

to its two-magnet configuration. In contrast, the T-GPEH exhibits the highest potential energy, with $E_p = 0$ only occurring at $y = 0$.

In this study, the widely adopted lumped-parameter modeling approach is used.[33–35] Incorporating the magnetic forces into consideration, the governing equations of the EQZS-GPEH are formulated as follows:

$$\begin{cases} M_{eff}\ddot{y} + C_{eff}\dot{y} + K_{eff}y + \theta V_p = F_a + F_m, \\ \theta\dot{y} = C_p\dot{V}_p + \dfrac{V_p}{R_L}, \end{cases} \tag{1}$$

where y is the displacement of the bluff body, M_{eff}, C_{eff}, and K_{eff} are the equivalent mass, damping coefficient, and stiffness, respectively. F_a is the aerodynamic force, and F_m is the magnetic force generated by the special five-magnet configuration. θ stands for the electromechanical coupling coefficient, C_p represents the clamped capacitance of the piezoelectric transducer, V_p is the output voltage across the load resistance R_L. Based on the quasi-steady theory, the aerodynamic force F_a can be empirically expressed as a polynomial function:[36]

$$F_a = 0.5\rho U^2 DL\sum_{i=1}^{n} A_i\left(\frac{\dot{y}}{U}\right)^i, \tag{2}$$

where ρ represents the fluid density, U is the wind speed, A_i ($i = 1, 3, 5, \ldots$) denotes the aerodynamic force coefficients, which can be determined from the experimental data at specified attack angles using the least squares method.[37] The dipole–dipole model[38] is utilized to qualitatively calculate the potential energy between magnet A and magnet B:

$$U_m = -\boldsymbol{B}_{BA}\cdot\boldsymbol{m}_A = \frac{\mu_0}{4\pi}\nabla\left(\frac{\boldsymbol{m}_B\cdot\boldsymbol{r}_{BA}}{r_{BA}^3}\right)\cdot\boldsymbol{m}_A, \tag{3}$$

where ∇ is the gradient operator;[39,40] $\boldsymbol{B}_{BA}$ represents the magnetic field generated by magnet A at the location of magnet B; $\boldsymbol{m}_A$ and $\boldsymbol{m}_B$ are the magnetic moments of magnets A and B, respectively; μ_0 is the vacuum permeability; $\boldsymbol{r}_{BA}$ is the vector from the magnetic moment source of magnet B to that of magnet A, with $r_{BA} = \sqrt{y^2 + d_1^2}$ denoting its magnitude. Hence, the magnetic force on magnet B exerted by magnet A, $\boldsymbol{F}_{BA}$, can be derived from Eq. (3):

$$\begin{aligned} \boldsymbol{F}_{BA} &= -\nabla U_m = -\frac{\mu_0}{4\pi}\nabla\left[\left(\nabla\frac{\boldsymbol{m}_B\cdot\boldsymbol{r}_{BA}}{r_{BA}^3}\right)\cdot\boldsymbol{m}_A\right] \\ &= \frac{3\mu_0 m_B m_A}{4\pi r_{BA}^4}\begin{bmatrix}(\hat{\boldsymbol{m}}_B\cdot\hat{\boldsymbol{m}}_A)\hat{\boldsymbol{r}}_{BA} + (\hat{\boldsymbol{m}}_B\cdot\hat{\boldsymbol{r}}_{BA})\hat{\boldsymbol{m}}_A + (\hat{\boldsymbol{m}}_A\cdot\hat{\boldsymbol{r}}_{BA})\hat{\boldsymbol{m}}_B \\ -5(\hat{\boldsymbol{m}}_B\cdot\hat{\boldsymbol{r}}_{BA})(\hat{\boldsymbol{m}}_A\cdot\hat{\boldsymbol{r}}_{BA})\hat{\boldsymbol{r}}_{BA}\end{bmatrix}, \end{aligned} \tag{4}$$

where m_B and m_A are the magnitudes of $\boldsymbol{m}_B$ and $\boldsymbol{m}_A$, respectively. $\hat{\boldsymbol{m}}_B$, $\hat{\boldsymbol{m}}_A$, $\hat{\boldsymbol{r}}_{BA}$ are the unit vectors of $\boldsymbol{m}_B$, $\boldsymbol{m}_A$, and $\boldsymbol{r}_{BA}$, respectively. In our study, $\hat{\boldsymbol{m}}_B\cdot\hat{\boldsymbol{m}}_A = -1$, since $\boldsymbol{m}_A$ is parallel to $\boldsymbol{m}_B$; $\hat{\boldsymbol{m}}_B\cdot\hat{\boldsymbol{r}}_{BA} = \cos\alpha$, α is the angle between $\boldsymbol{m}_B$ and $\boldsymbol{r}_{BA}$, and $\hat{\boldsymbol{m}}_A\cdot\hat{\boldsymbol{r}}_{BA} = -\cos\alpha$. Consequently, $\boldsymbol{F}_{BA}$ can be simplified as:

$$\boldsymbol{F}_{BA} = \frac{3\mu_0 m_B m_A}{4\pi r_{BA}^4}\left(-\hat{\boldsymbol{r}}_{BA} + \hat{\boldsymbol{m}}_A\cos\alpha - \hat{\boldsymbol{m}}_B\cos\alpha + 5\cos^2\alpha\hat{\boldsymbol{r}}_{BA}\right). \tag{5}$$

The projections of $\boldsymbol{m}_A$ and $\boldsymbol{m}_B$ along the y-axis are 0. Hence, the y-axis component $\boldsymbol{F}_{BA}$, denoted as $\boldsymbol{F}_{y1}$, is given as:

$$\boldsymbol{F}_{y1} = \frac{3\mu_0 m_B m_A}{4\pi r_{BA}^4}\left(5\cos^2\alpha\hat{\boldsymbol{r}}_{BA} - \hat{\boldsymbol{r}}_{BA}\right)\sin\alpha, \tag{6}$$

where $\cos\alpha = d_1/r_{BA}$, $\sin\alpha = y/r_{BA}$. Then, the magnitude of $\boldsymbol{F}_{y1}$ can be derived as:

$$\begin{aligned} F_{y1} &= \frac{3\mu_0 m_B m_A}{4\pi r_{BA}^4}(5\cos^2\alpha - 1)\sin\alpha \\ &= \frac{3\mu_0 m_B m_A}{4\pi r_{BA}^4}\left(\frac{5d_1^2}{r_{BA}^2} - 1\right)\frac{y}{r_{BA}} \\ &= \frac{3\mu_0 m_B m_A}{4\pi}\left[\frac{5yd_1^2}{(y^2+d_1^2)^{\frac{7}{2}}} - \frac{y}{(y^2+d_1^2)^{\frac{5}{2}}}\right]. \end{aligned} \tag{7}$$

Similarly, the y-axis component of the magnetic force generated by the bottom magnets, denoted as F_b, can be expressed as:[33]

$$\begin{aligned} F_b &= F_{b1} + F_{b2} \\ &= \frac{3\mu_0 m_B m_A}{4\pi}\left\{\begin{aligned}&\frac{5(y-0.5h_1)d_2^2}{\left[(y-0.5h_1)^2+d_2^2\right]^{\frac{7}{2}}} - \frac{y-0.5h_1}{\left[(y-0.5h_1)^2+d_2^2\right]^{\frac{5}{2}}} \\ &+\frac{5(y+0.5h_1)d_2^2}{\left[(y+0.5h_1)^2+d_2^2\right]^{\frac{7}{2}}} - \frac{y+0.5h_1}{\left[(y+0.5h_1)^2+d_2^2\right]^{\frac{5}{2}}}\end{aligned}\right\}, \end{aligned} \tag{8}$$

where F_{b1} is the y-axis component of the magnetic force between magnet C and magnet D, F_{b2} is the y-axis component of the magnetic force between magnet C and magnet E.

The total magnetic force generated by the five-magnet configuration, denoted as F_m, can be eventually expressed as:

$$F_m = F_{y1} + F_b. \tag{9}$$

By substituting Eqs. (7)–(9) into Eq. (1), the governing equations of the proposed EQZS-GPEH are derived. Furthermore, the governing equations of the CQZS-GPEH and T-GPEH can be obtained by setting $F_b = 0$ and $F_m = 0$, respectively.

To assess the performance of the proposed EQZS-GPEH, experimental tests were conducted in a large circulating wind tunnel. The voltage outputs from the three GPEH prototypes were measured using a dual-channel oscilloscope (Analog Discovery 2), and their displacement responses were gauged using a high-resolution Doppler laser sensor (SG6150).[33]

Figures 2(a) and 2(b) show the RMS voltage output (V_{rms}) and displacement amplitude (Y_{max}) of the three GPEHs vs wind speed. The T-GPEH exhibits the highest onset wind speed of 3.964 m/s and achieves a maximum V_{rms} of 31.67 V and Y_{max} of 9.65 mm at $U = 5.182$ m/s. In comparison, the CQZS-GPEH and EQZS-GPEH exhibit lower onset wind speeds (2.92 and 2.224 m/s) and higher voltage outputs (38.56 and 52.18 V). Their Y_{max} values (10.88 and 18.16 mm) also exceed that of the T-GPEH. These results demonstrate the superior performance of the EQZS-GPEH, especially at lower wind speeds.

Figure 2(c) presents the time-history voltage responses of the three GPEHs at three different wind speeds. At $U = 2.224$ m/s, the EQZS-GPEH exhibits an unstable voltage response. This voltage fluctuation is primarily attributed to the nonlinear magnetic force, whose

08 January 2026 14:58:50

Published under an exclusive license by AIP Publishing

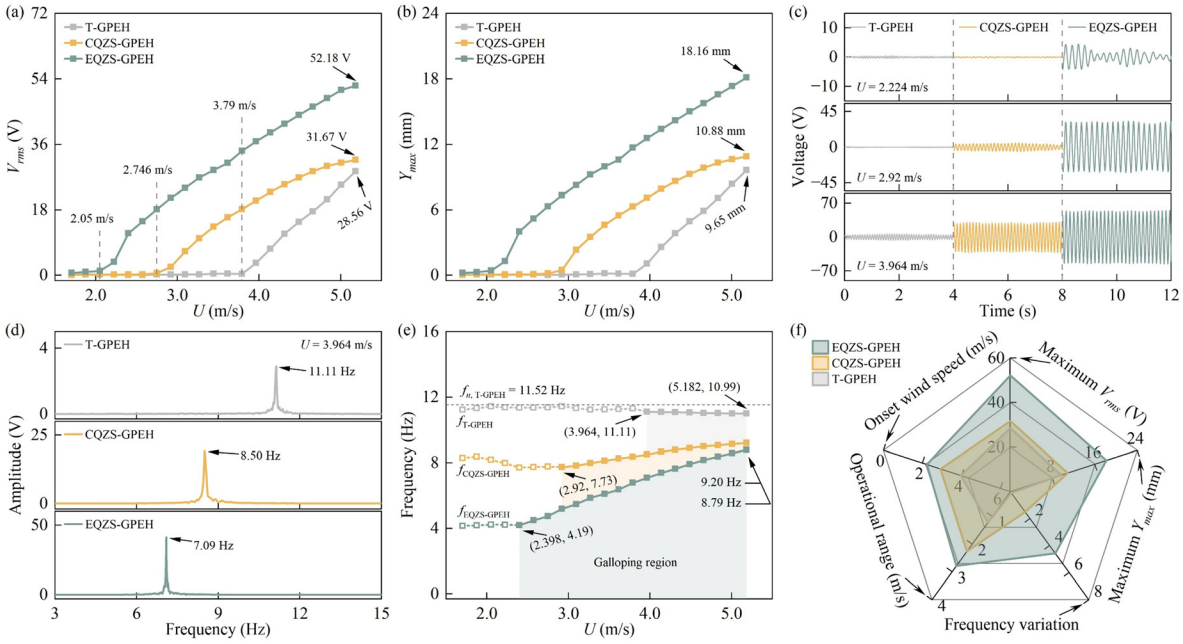

FIG. 2. (a) Open-circuit RMS voltage (V_{rms}) of the three GPEHs; (b) maximum displacement response (Y_{max}) vs wind speed; (c) time-history voltage outputs at three different wind speeds; (d) spectra at $U = 3.964$ m/s; (e) vibration frequencies vs wind speed; and (f) comprehensive comparison of the three GPEHs.

magnitude is pretty sensitive to the distance between the magnets.[41] Furthermore, the magnetic interaction introduces strong nonlinearity into the effective stiffness of the system, and this nonlinearity becomes more pronounced with variations in the wind speed.[42] As a result, even minor fluctuations in wind speed at $U = 2.224$ m/s can affect the system's dynamic response, leading to voltage instability in the EQZS-GPEH.

Figure 2(d) shows the voltage spectrograms of the three GPEHs at $U = 3.964$ m/s. Vibration frequencies of the EQZS-GPEH, CQZS-GPEH, and T-GPEH are determined to be 7.09, 8.50, and 11.11 Hz, respectively, through fast Fourier transform (FFT) analysis.[43] The reduced vibration frequency of the EQZS-GPEH is attributed to the magnetic forces, which counteract the elastic restoring force of the cantilever beam, thereby softening the structure. Furthermore, as demonstrated in Fig. 2(e), the vibration frequency of the EQZS-GPEH ($f_{EQZS\text{-}GPEH}$) decreases to 4.19 Hz when $U = 2.398$ m/s due to the significant stiffness reduction caused by the softening effect of the magnetic force. As the wind speed increases, Y_{max} gradually rises, enabling the EQZS-GPEH to overcome the magnetic softening effect, resulting in a gradual increase of $f_{EQZS\text{-}GPEH}$.

As shown in Fig. 2(e), the vibration frequency of the T-GPEH ($f_{T\text{-}GPEH}$) decreases slightly with wind speed, from 11.11 to 10.99 Hz, due to the aerodynamic negative damping.[48] The CQZS-GPEH, with a single magnet pair, has a stiffness between the T-GPEH and EQZS-GPEH: its frequency drops to 7.73 Hz at $U = 2.92$ m/s and rises to 9.18 Hz at $U = 5.182$ m/s. Figure 2(f) compares the three GPEHs in terms of operational range, onset wind speed, V_{rms}, Y_{max}, and frequency variation. The EQZS-GPEH exhibits the broadest operational bandwidth (2.398–5.182 m/s), lowest onset wind speed (2.224 m/s), largest V_{rms} (52.18 V), highest Y_{max} (18.16 mm), and greatest frequency variation (4.58 Hz), confirming it as the optimal design for efficient wind energy harvesting.

As shown in Fig. 3(a), at the wind speed of 4.834 m/s, the RMS voltage outputs V_{rms} of all three GPEHs increase as the load resistance R_L rises, with the EQZS-GPEH consistently exhibiting higher V_{rms} than the other two. Figure 3(b) shows the RMS power output (P_{rms}) with the change of load resistance at $U = 4.834$ m/s, where $P_{rms} = {V_{rms}}^2/R_L$. Based on these results, the optimal power outputs of the EQZS-GPEH, CQZS-GPEH, and T-GPEH are determined to be 1.55 mW, 0.64 mW, and 0.39 mW at $R_L = 0.7$ MΩ, respectively. As shown in Fig. 3(c), the P_{rms} of the EQZS-GPEH and CQZS-GPEH are at least 237.36% and 38.01% higher than that of the T-GPEH, respectively.

Subsequently, capacitor charging tests were conducted with the results presented in Fig. 3(d). After 480 s, the voltage across all three capacitors exceeded 5.0 V, with a clear upward trend. Figure 3(e) depicts the relationship between vibration frequency (f) and wind speed (U) for each GPEH, fitted from frequency variation data, with all three devices achieving a high fit quality ($R^2 > 0.97$). Here, the indicator of fit quality R^2 can be calculated by

$$R^2 = 1 - \frac{\sum_{i=1}^{n} \left(f_i - \hat{f}_i\right)^2}{\sum_{i=1}^{n} \left(f_i - \bar{f}\right)^2}, \tag{10}$$

where f_i is the true value of vibration frequency, $\hat{f}_i$ is the predicted vibration frequency, $\bar{f}$ is the average value of f_i, and n is the sample size. R^2 reflects the fit quality between the regression line and actual values. The T-GPEH's vibration frequency basically remains constant when wind speed changes. Hence, it cannot distinguish between

08 January 2026 14:58:50

Published under an exclusive license by AIP Publishing

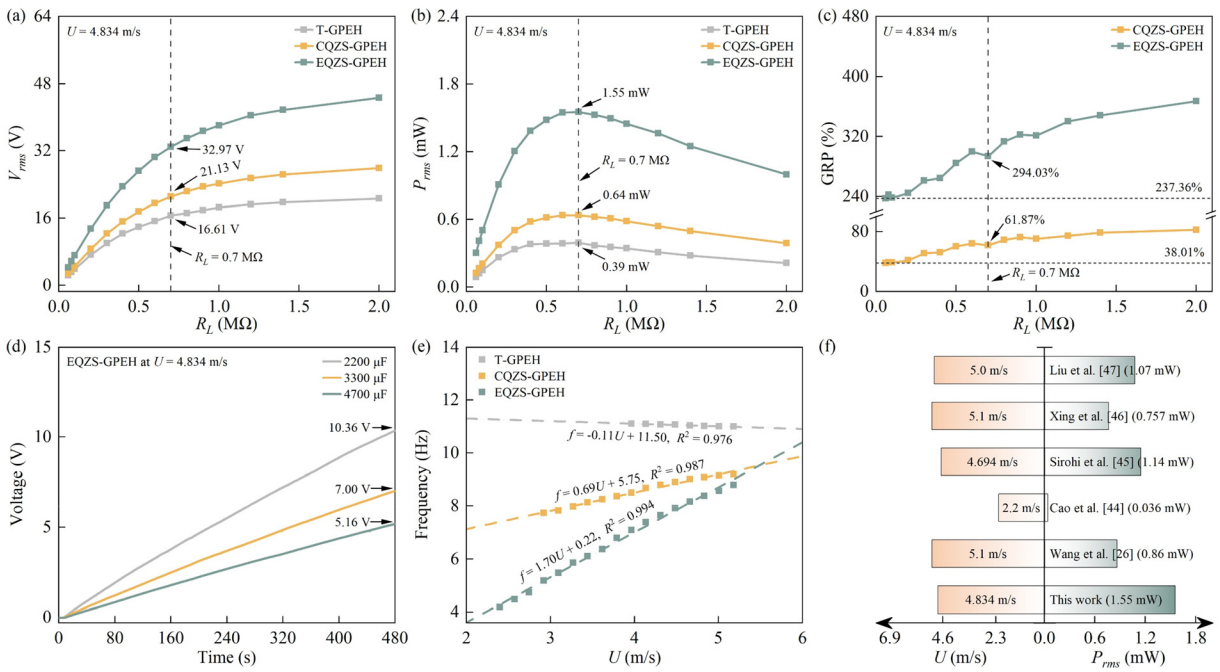

FIG. 3. (a) RMS voltage (V_{rms}) vs load resistance (R_L) at $U = 4.834$ m/s; (b) RMS power (P_{rms}) vs load resistance (R_L) at $U = 4.834$ m/s; (c) growth rate of P_{rms} (GRP) of the CQZS-GPEH and EQZS-GPEH compared with the T-GPEH at $U = 4.834$ m/s; (d) capacitor charging performance of the EQZS-GPEH at $U = 4.834$ m/s; (e) fitted linear relationship between vibration frequency (f) and wind speed (U) for the three GPEHs with corresponding indicator of fit quality (R^2); and (f) performance comparison of the proposed EQZS-GPEH with previously reported harvesters.[26,44–47]

different wind speeds. In comparison, the EQZS-GPEH exhibits the largest frequency variation and the highest fit quality ($R^2 = 0.994$), identifying it as the most promising candidate for the wind speed sensing application. Hence, the EQZS-GPEH is used for the wind speed sensing application. A comprehensive comparison between different designs is shown in Fig. 3(f), further highlighting the superiority of the proposed EQZS-GPEH.

The application of the EQZS-GPEH for self-powered wind speed sensing is shown in Fig. 4. The EQZS-GPEH powers an analog-to-digital converter (ADC) circuit that measures its voltage to estimate wind speed; together, they form the self-powered ADC (SP-ADC) system. The circuit includes a voltage regulator, rectifier, storage capacitor, energy management unit (LTC3588-1), and microcontroller (nRF52832), with details shown in Figs. 4(b) and 4(e). Figure 4(f) presents the PCB implementation, and the components are listed in Table II.

The AC voltage from the EQZS-GPEH is first regulated, with the low-amplitude voltage signal across resistor R_1 fed to MCU pins P04 and P05 for sampling, frequency calculation, and wind speed sensing. To avoid signal clipping during ADC sampling, a protection circuit composed of a filtering capacitor (C_0) and two Zener diodes (D_0, D_1) limits R_1 voltage to a maximum of 1.8 V. Meanwhile, the AC voltage across resistor R_0 is rectified to charge the energy storage capacitor (C_{STO}), with a parallel switch to dissipate excess energy. The undervoltage lockout (UVLO) function of the EMU allows energy to accumulate in C_{STO}, and its buck converter delivers power once V_{STO} reaches a set threshold, ensuring a stable supply to the MCU.

The application test was conducted in the circulating wind tunnel, as shown in Fig. 5(a). First of all, as shown in Fig. 5(d), when operating at a wind speed of 4.486 m/s, the EQZS-GPEH lit up 66 LEDs, spelling out "HKUST(GZ)." To further demonstrate its potential, a more challenging application was conducted to evaluate the SP-ADC system, which comprises the EQZS-GPEH and ADC circuit, for wind speed sensing. Given that the vibration frequency of the EQZS-GPEH is around or below 10 Hz, the SP-ADC system operated at a sampling frequency of 100 Hz to ensure accurate voltage signal acquisition.

Figure 5(f) shows that during the initial start of the SP-ADC system, C_{STO} was first charged to 5.10 V. The EMU then regulated the capacitor voltage to 3.35 V. Once the sampling operation began, electrical energy stored in C_{STO} was delivered to the MCU, causing V_{STO} to drop to 3.73 V within 2.1 s. After the SP-ADC system completed the sampling operation, the EMU's UVLO function was activated, and the buck converter was disabled. Subsequently, energy continued to accumulate in C_{STO} to support the next MCU operation. At $U = 4.486$ m/s, the system maintained an operation cycle interval of approximately 163.0 s, with the interval decreasing as the wind speed increased. To further boost the power output and reduce the cold-start time, future work will focus on improving the efficiency and robustness of the system by incorporating more advanced interface circuits such as self-powered synchronous charge extraction (SP-SECE)[49] and self-powered synchronized switch harvesting on inductor (SP-SSHI) circuits.[50]

Based on the linear relationship between wind speed and the vibration frequency of the EQZS-GPEH, the wind speed (U) can be estimated using the fitted curve shown in Fig. 3(e),

08 January 2026 14:58:50

Published under an exclusive license by AIP Publishing

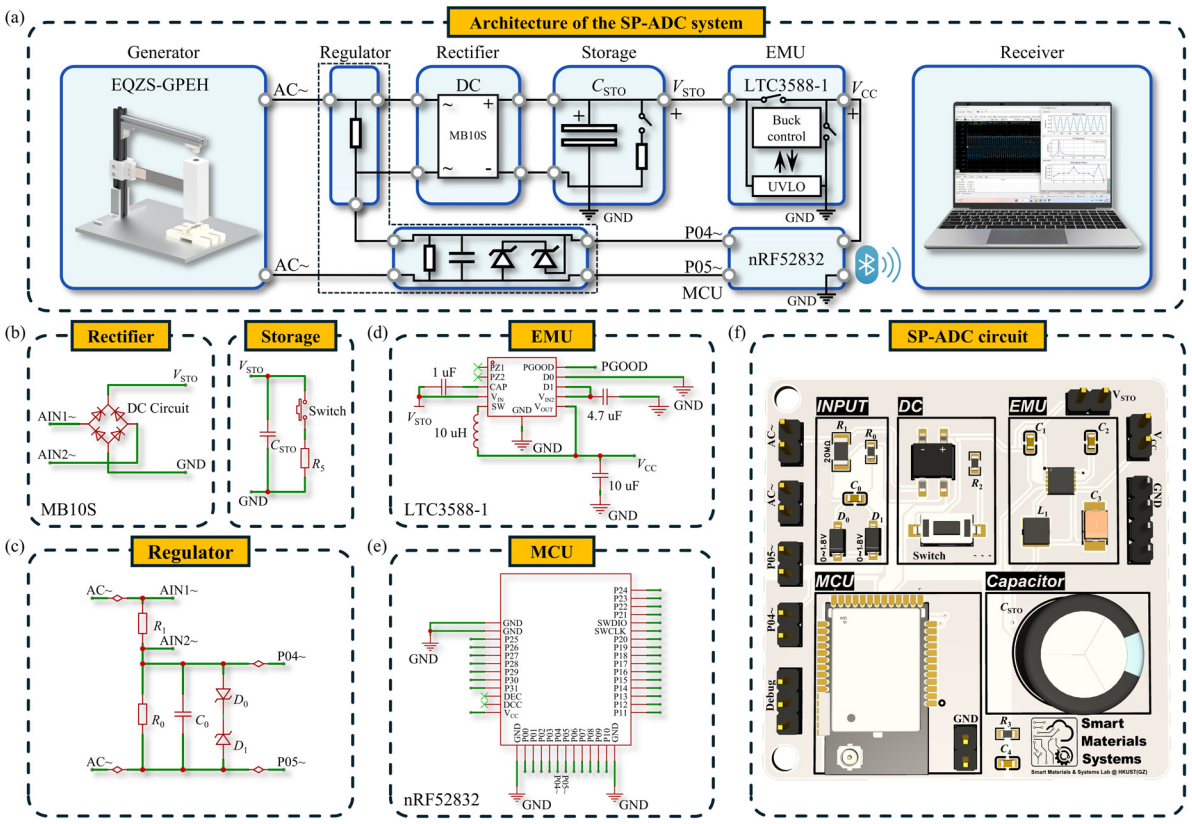

FIG. 4. (a) The architecture of the SP-ADC system; (b)–(e) circuit diagram and detailed illustration of different components of the SP-ADC circuit; and (f) the printed circuit board (PCB) implemented SP-ADC circuit.

$$U = 0.59f - 0.11. \tag{11}$$

Figures 5(g)–5(i) show that the SP-ADC system provides results highly consistent with those of a commercial oscilloscope, achieving a small relative error of less than 5% for vibration frequency, wind speed, and RMS voltage across R_1. To further validate, the vibration frequency analyzed by the fast Fourier transform (FFT) method is plotted in Fig. 5(g), and the estimated wind speed is plotted in Fig. 5(h). Both the wind speed and vibration frequency identified by the SP-ADC system exhibit relative errors below 5%. Furthermore, Figs. 5(j) and 5(k) show the time-history voltage across R_1 and its spectrum at $U = 4.486$ m/s, further confirming the high accuracy of the SP-ADC system. As the cantilever beam undergoes repeated cyclic loading, long-term operation may induce fatigue in both structural and piezoelectric components. Therefore, to support long-term use, future work may consider adopting cantilever beams with higher fatigue limits, durable piezoelectric materials, and magnets with high coercivity and environmental stability.

TABLE II. The electronic elements used in building the SP-ADC circuit.

Components	Value/model
R_0	20 MΩ
R_1	1 MΩ
C_0	10 μF
D_0, D_1	SZMMSZ4678T1G
Rectifier	MB10S
C_{STO}	3300 μF
R_5	1 kΩ
Switch	TS1305-TZ50HBM

In this work, we proposed an enhanced quasi-zero-stiffness galloping piezoelectric energy harvester (EQZS-GPEH) that features a five-magnet configuration to reduce cantilever beam stiffness and create an expanded QZS region over a larger displacement range. Experimental validation that this expanded QZS significantly improves energy harvesting performance. The EQZS-GPEH achieved a maximum RMS voltage of 52.18 V, a displacement amplitude of 18.16 mm, and a power output of 1.55 mW at $R_L = 0.7$ MΩ and $U = 4.834$ m/s, representing a 294% improvement over the traditional GPEH (T-GPEH) and a 142% improvement over the conventional QZS-GPEH (CQZS-GPEH). In addition, the harvester demonstrated excellent sensing capability, exhibiting a highly linear relationship between vibration frequency and wind speed ($R^2 = 0.994$), providing the possibility for wind speed estimation. Leveraging this characteristic, a

08 January 2026 14:58:50

Published under an exclusive license by AIP Publishing

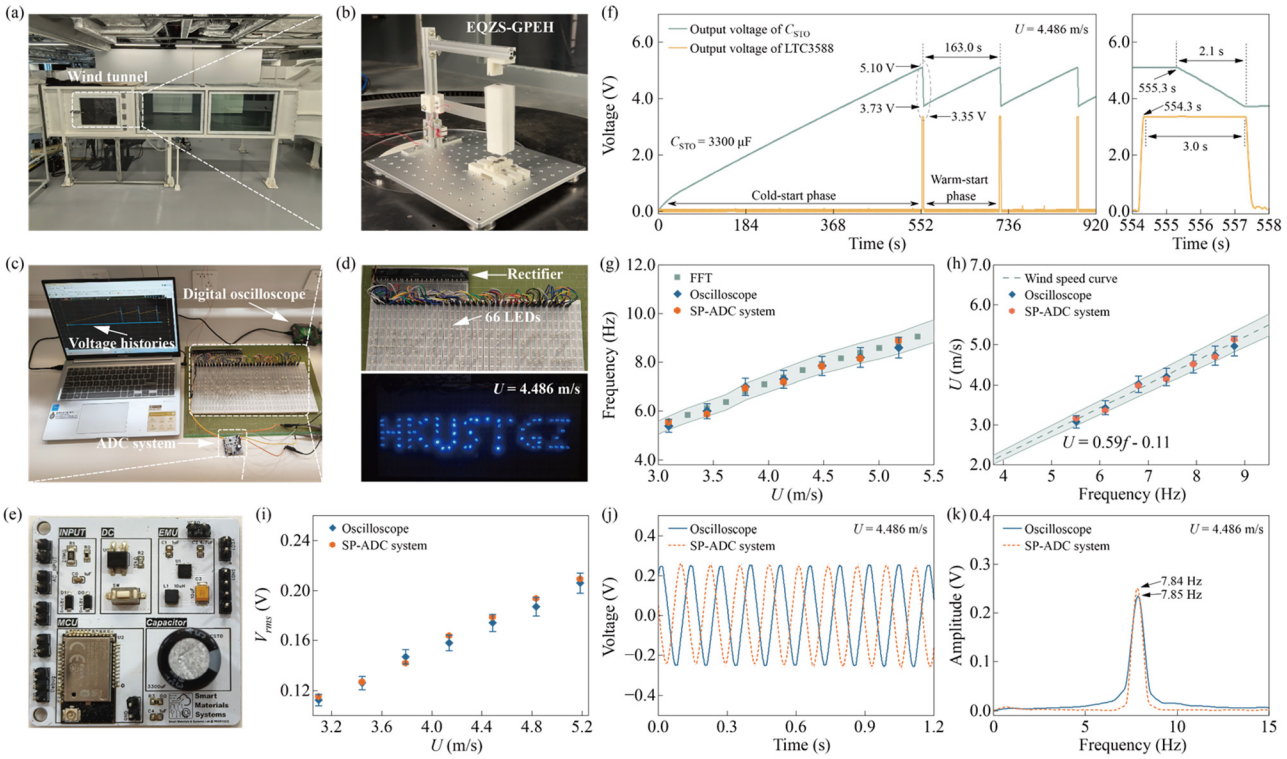

FIG. 5. (a) Wind tunnel test section; (b) prototyped EQZS-GPEH in the wind tunnel; (c) experiment setup; (d) EQZS-GPEH lighting up 66 LEDs at $U = 4.486$ m/s; (e) enlarged view of the SP-ADC circuit; (f) time-history voltage from the SP-ADC system at $U = 4.486$ m/s; (g) vibration frequency from the FFT, oscilloscope and SP-ADC system; (h) wind speed estimated by the oscilloscope and the SP-ADC system; (i) RMS voltage on R_1 sampled by the digital oscilloscope and the SP-ADC system; and (j) voltage histories on R_1 and (k) the corresponding spectra sampled by the digital oscilloscope and the SP-ADC system at $U = 4.486$ m/s.

self-powered analog-to-digital converter (SP-ADC) system powered solely by the EQZS-GPEH was developed, achieving wind speed measurements with a relative error of <5% compared to reference instrumentation. These findings demonstrate the EQZS-GPEH as a reliable and scalable energy harvesting solution capable of powering autonomous sensor nodes and supporting long-term, maintenance-free environmental monitoring, positioning it as an enabling technology for widespread IoT infrastructure deployment. Future studies may focus on validating the long-term stability and reliability of the SP-ADC system under real outdoor conditions, particularly in the presence of fluctuating wind gusts and atmospheric turbulence. Moreover, to improve the accuracy of the magnet force model, more precise modified dipole models could also be employed in future studies for a comprehensive theoretical analysis.

This study was partially supported by the National Natural Science Foundation of China (Grant No. 52305135), the Guangzhou Municipal Science and Technology Bureau (Grant Nos. SL2023A03J00869 and SL2023A04J01741), and the Guangdong Provincial Project (Grant No. 2023QN10L545).

The authors thank the Bio-Inspired Engineering Research Facility (BIO-IERF) in HKUST(GZ) for providing the essential research facilities. Special thanks are extended to Mr. Jiaming Wu and Mr. Lixiang Wu for assistance with this work.

AUTHOR DECLARATIONS

Conflict of Interest

The authors have no conflicts to disclose.

Author Contributions

Ye Zhang and Yawei Wang contributed equally to this work.

Ye Zhang: Data curation (equal); Formal analysis (equal); Investigation (equal); Methodology (equal); Software (lead); Validation (equal); Visualization (lead); Writing – original draft (equal). **Yawei Wang:** Conceptualization (supporting); Data curation (equal); Formal analysis (equal); Investigation (equal); Methodology (equal); Software (supporting); Validation (equal); Visualization (supporting). **Yaozi Zheng:** Data curation (supporting); Formal analysis (supporting); Investigation (supporting). **Chunbo Lan:** Conceptualization (supporting); Investigation (equal); Methodology (equal); Writing – review & editing (supporting). **Guobiao Hu:** Conceptualization (lead); Formal analysis (equal); Funding acquisition (lead); Investigation (equal); Methodology (equal); Project administration (lead); Supervision (lead); Writing – review & editing (lead).

DATA AVAILABILITY

The data that support the findings of this study are available from the corresponding author upon reasonable request.

08 January 2026 14:58:50

Published under an exclusive license by AIP Publishing

REFERENCES

[1]M. Gotte and P. S. R. Sreekanth, J. Mater. Sci. **60**(20), 8253 (2025).
[2]X. Zhao, H. Askari, and J. Chen, Joule **5**(6), 1391 (2021).
[3]W. Deng, Y. Zhou, A. Libanori, G. Chen, W. Yang, and J. Chen, Chem. Soc. Rev. **51**(9), 3380 (2022).
[4]M. Piñuela, P. D. Mitcheson, and S. Lucyszyn, IEEE Trans. Microwave Theory Tech. **61**(7), 2715 (2013).
[5]F. Deng, X. H. Yue, X. Y. Fan, S. P. Guan, Y. Xu, and J. Chen, IEEE Internet Things J. **6**(1), 918 (2019).
[6]Y. Z. Li, Y. W. Wang, Y. H. Li, X. Z. Peng, D. Li, X. Xia, X. Li, Y. L. Zi, and G. B. Hu, Appl. Phys. Lett. **126**(2), 023902 (2025).
[7]Y. W. Wang, H. X. Du, H. Y. Yang, Z. Y. Xi, C. Zhao, Z. A. Qian, X. Y. Chuai, X. Z. Peng, H. Y. Yu, Y. Zhang, X. Li, G. B. Hu, H. Wang, and M. Y. Xu, Nat. Commun. **15**(1), 6834 (2024).
[8]T. Sarpkaya, J. Fluids Struct. **19**(4), 389 (2004).
[9]G. V. Parkinson and P. P. Sullivan, J. Wind Eng. Ind. Aerodyn. **4**(3-4), 253 (1979).
[10]Z. Y. Li, S. X. Zhou, and Z. C. Yang, Int. J. Mech. Syst. Dyn. **2**(1), 82 (2022).
[11]S. Francis and A. Swain, Ocean Eng. **312**, 119290 (2024).
[12]X. X. Xue, H. J. Xiang, Y. M. Ci, and J. Y. Wang, Energy **320**, 135135 (2025).
[13]J. L. Wang, S. K. Sun, G. B. Hu, Y. W. Yang, L. H. Tang, P. Li, and G. J. Zhang, Energy Convers. Manage. **243**, 114414 (2021).
[14]I. Major, P. J. Tan, and A. Abolfathi, Smart Mater. Struct. **33**(10), 105031 (2024).
[15]Q. Liu, W. Y. Qin, Z. Y. Zhou, M. J. Shang, and H. L. Zhou, Energy **284**, 129330 (2023).
[16]Z. Y. Zhou, D. Cao, H. B. Huang, and W. Y. Qin, Mech. Syst. Signal Proc. **209**, 111124 (2024).
[17]J. W. Kan, W. L. Liao, S. Y. Wang, S. Chen, X. Huang, and Z. H. Zhang, Energy Convers. Manage. **240**, 114250 (2021).
[18]Q. Bai, C. Z. Gan, T. Zhou, Z. C. Du, J. H. Wang, Q. Wang, K. X. Wei, and H. X. Zou, Energy Convers. Manage. **306**, 118323 (2024).
[19]Q. D. Lin, J. X. Zhou, K. Wang, C. Q. Cai, and Q. Wang, Nonlinear Dyn. **113**(19), 25459 (2025).
[20]K. Li, Z. C. Yang, and S. X. Zhou, Smart Mater. Struct. **29**(8), 085045 (2020).
[21]X. F. Geng, H. Ding, X. J. Jing, X. Y. Mao, K. X. Wei, and L. Q. Chen, Mech. Syst. Signal Proc. **185**, 109813 (2023).
[22]J. Bian and X. J. Jing, Nonlinear Dyn. **101**(4), 2195 (2020).
[23]T. T. Chen, K. Wang, L. Cheng, H. B. Pan, H. C. Cui, and J. X. Zhou, Commun. Nonlinear Sci. **133**, 107863 (2024).
[24]Q. Wang, J. X. Zhou, K. Wang, Q. D. Lin, D. L. Xu, and G. L. Wen, Int. J. Mech. Sci. **250**, 108284 (2023).
[25]C. P. Liu and X. J. Jing, Mech. Syst. Signal Proc. **234**, 112814 (2025).
[26]J. W. Wang, B. W. Tang, and W. Tan, Smart Mater. Struct. **33**(2), 025003 (2024).
[27]H. R. Zhang, L. A. Zhang, Y. B. Wang, X. H. Yang, R. J. Song, and W. T. Sui, Smart Mater. Struct. **31**(6), 065007 (2022).
[28]S. Chen and L. Y. Zhao, Appl. Energy **331**, 120423 (2023).
[29]B. Su, T. Guo, and M. M. Alam, Appl. Energy **389**, 125771 (2025).
[30]J. L. Scornec, B. Guiffard, R. Seveno, V. L. Cam, and S. Ginestar, Renewable Energy **184**, 551 (2022).
[31]L. P. He, Y. Hou, X. J. Liu, R. W. Liu, B. J. Yu, H. Huang, and J. Q. Lin, Smart Mater. Struct. **32**(10), 105008 (2023).
[32]H. X. Zou, L. C. Zhao, Q. Wang, Q. H. Gao, G. Yan, K. X. Wei, and W. M. Zhang, Nano Energy **95**, 106990 (2022).
[33]C. B. Lan, Y. Zhang, S. Wang, Y. Lu, Y. W. Wang, and G. B. Hu, Smart Mater. Struct. **34**(5), 055018 (2025).
[34]S. K. Al Nuaimi, V. C. Meesala, and M. R. Hajj, Appl. Phys. Lett. **115**(19), 193701 (2019).
[35]T. Tan and Z. Yan, Appl. Phys. Lett. **109**(25), 253902 (2016).
[36]G. Z. Gao and L. D. Zhu, J. Fluids Struct. **70**, 47 (2017).
[37]S. Jo, W. Sun, C. Son, and J. Seok, AIP Adv. **8**(9), 095309 (2018).
[38]X. Q. Ma, Z. Y. Li, H. Zhang, and S. X. Zhou, Mech. Syst. Signal Proc. **187**, 109924 (2023).
[39]K. W. Yung, P. B. Landecker, and D. D. Villani, Phys. Separ. Sci. Eng. **9**(1), 39 (1998).
[40]D. Tan, Y. G. Leng, and Y. J. Gao, Eur. Phys. J.: Spec. Top. **224**(14-15), 2839 (2015).
[41]K. Li, Z. C. Yang, Y. S. Gu, S. He, and S. X. Zhou, Smart Mater. Struct. **28**(1), 015020 (2019).
[42]H. G. Tian, X. B. Shan, X. Li, and J. L. Wang, Appl. Energy **340**, 120979 (2023).
[43]A. Luongo and G. Piccardo, J. Sound Vib. **214**(5), 915 (1998).
[44]D. Cao, W. Y. Qin, Z. Y. Zhou, and W. F. Du, Energy Convers. Manage. **318**, 118871 (2024).
[45]J. Sirohi and R. Mahadik, J. Vib. Acoust. **134**(1), 011009 (2012).
[46]J. T. Xing, M. Rezaei, H. L. Dai, and W. H. Liao, Appl. Phys. Lett. **122**(15), 153902 (2023).
[47]F. R. Liu, W. M. Zhang, Z. K. Peng, and G. Meng, Energy **183**, 92 (2019).
[48]J. H. G. Macdonald and G. L. Larose, J. Fluids Struct. **22**(2), 229 (2006).
[49]L. H. Tang and Y. W. Yang, Smart Mater. Struct. **20**(8), 085022 (2011).
[50]J. R. Liang and W. H. Liao, IEEE Trans. Ind. Electron. **59**(4), 1950 (2012).

08 January 2026 14:58:50

Published under an exclusive license by AIP Publishing